Coordinated Radiodiagnostics Of CMEs and Solar flares (CROCS)

Vratislav Krupar

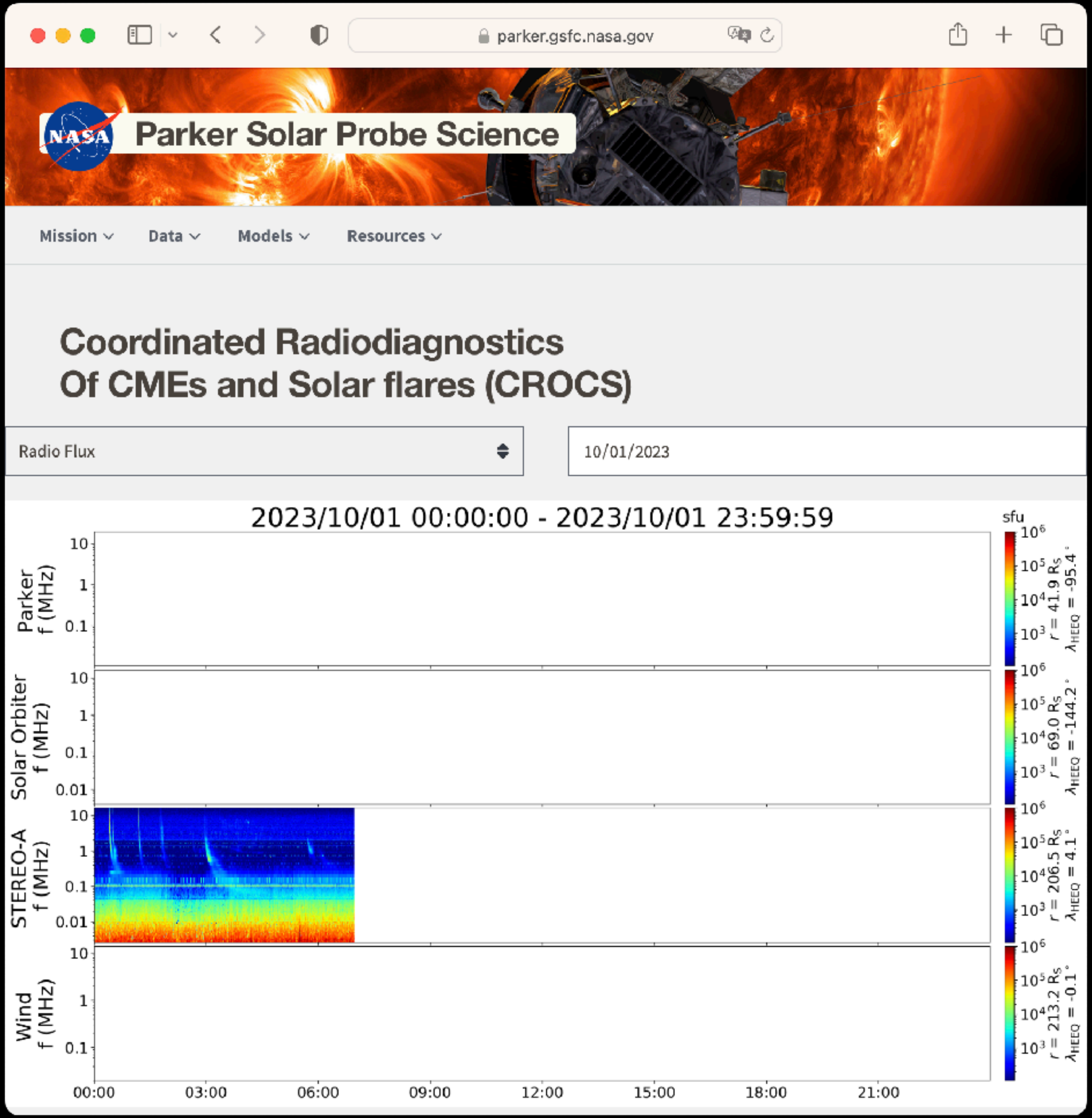

https://parker.gsfc.nasa.gov/crocs.html

2023/03/13 00:00:00 - 2023/03/13 23:59:59
sfu
Parker
f (MHz)
Solar Orbiter
f (MHz)
STEREO-A
f (MHz)
Wind
f (MHz)
r = 47.7 R_S
λ_HEEQ = -151.5°
r = 129.6 R_S
λ_HEEQ = -26.2°
r = 207.7 R_S
λ_HEEQ = -12.4°
r = 213.1 R_S
λ_HEEQ = -0.2°
00:00
03:00
06:00
09:00
12:00
15:00
18:00
21:00

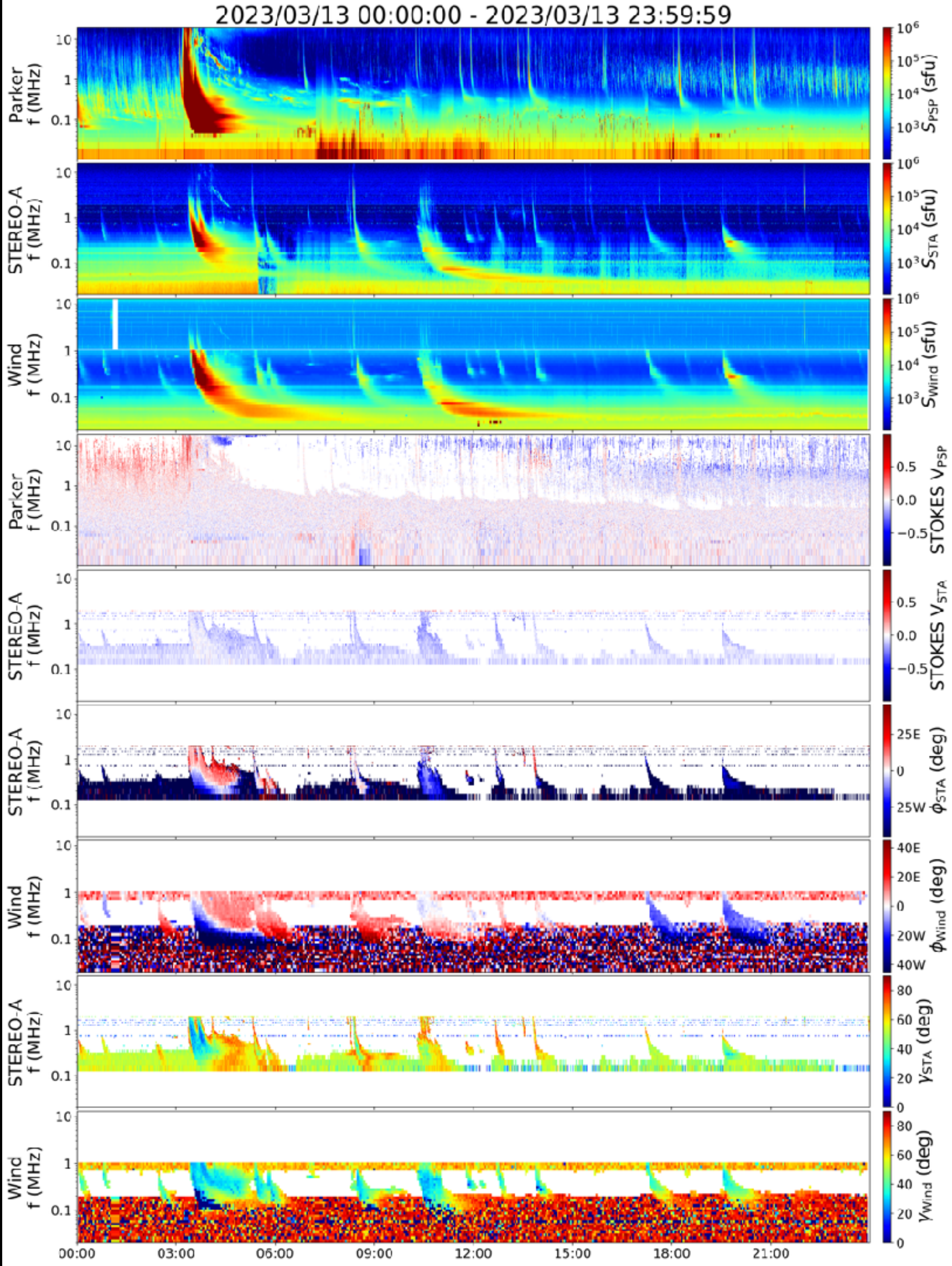

Parker	https://spdf.gsfc.nasa.gov/pub/data/psp/fields/l3/rfs_hfr/ https://spdf.gsfc.nasa.gov/pub/data/psp/fields/l3/rfs_lfr/
Solar Orbiter	https://spdf.gsfc.nasa.gov/pub/data/solar-orbiter/rpw/science/l2/hfr-surv/ https://spdf.gsfc.nasa.gov/pub/data/solar-orbiter/rpw/science/l2/tnr-surv/
STEREO	https://spdf.gsfc.nasa.gov/pub/data/stereo/ahead/l3/waves/hfr/ https://spdf.gsfc.nasa.gov/pub/data/stereo/ahead/l3/waves/lfr/
Wind	https://cdpp-archive.cnes.fr/ https://spdf.gsfc.nasa.gov/pub/data/wind/waves/rad1_l3_df/

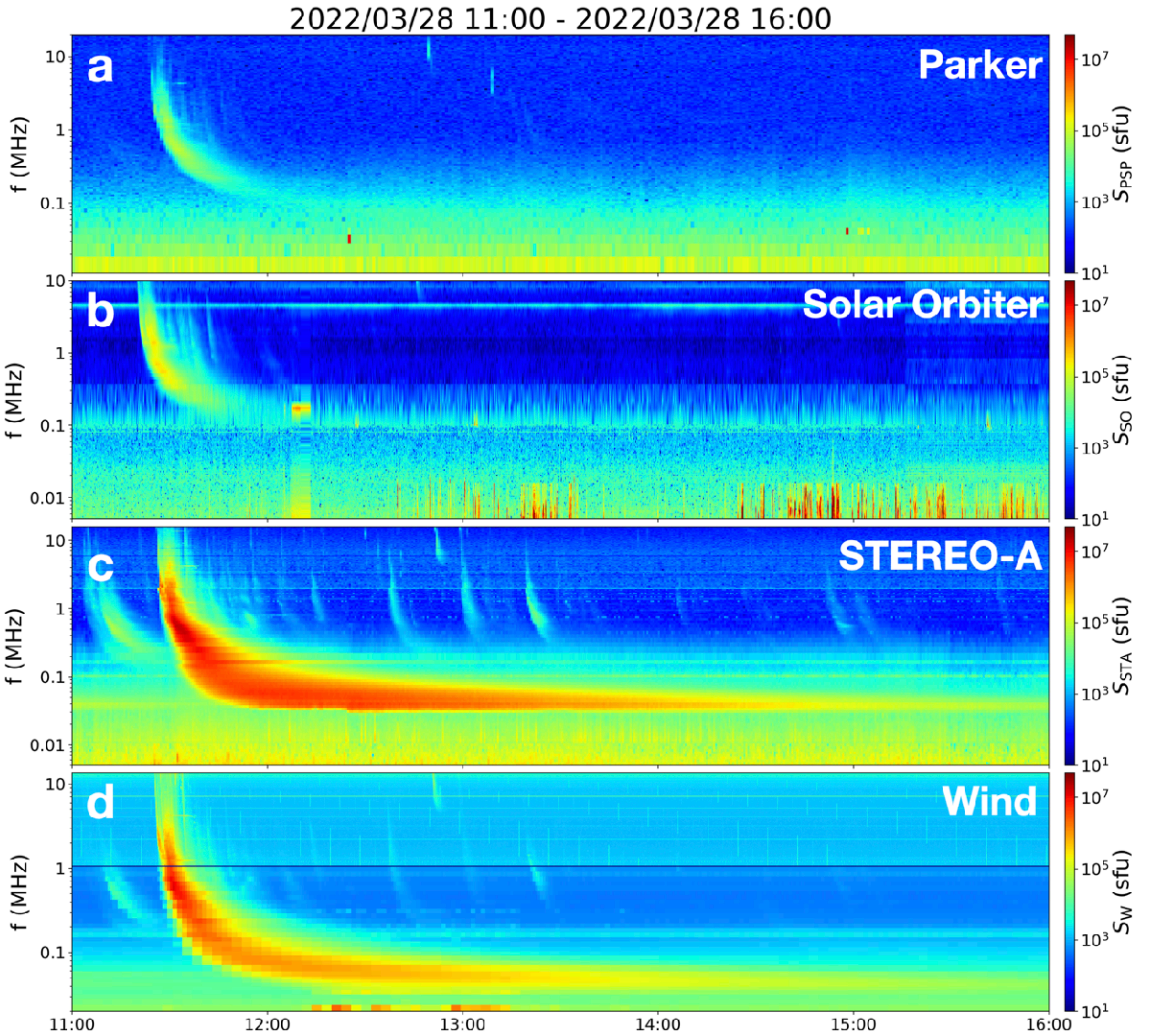
2022/03/28 11:00 - 2022/03/28 16:00
a
Parker
b
Solar Orbiter
c
STEREO-A
d
Wind
f (MHz)
S_{PSP} (sfu)
S_{SO} (sfu)
S_{STA} (sfu)
S_{W} (sfu)
11:00
12:00
13:00
14:00
15:00
16:00

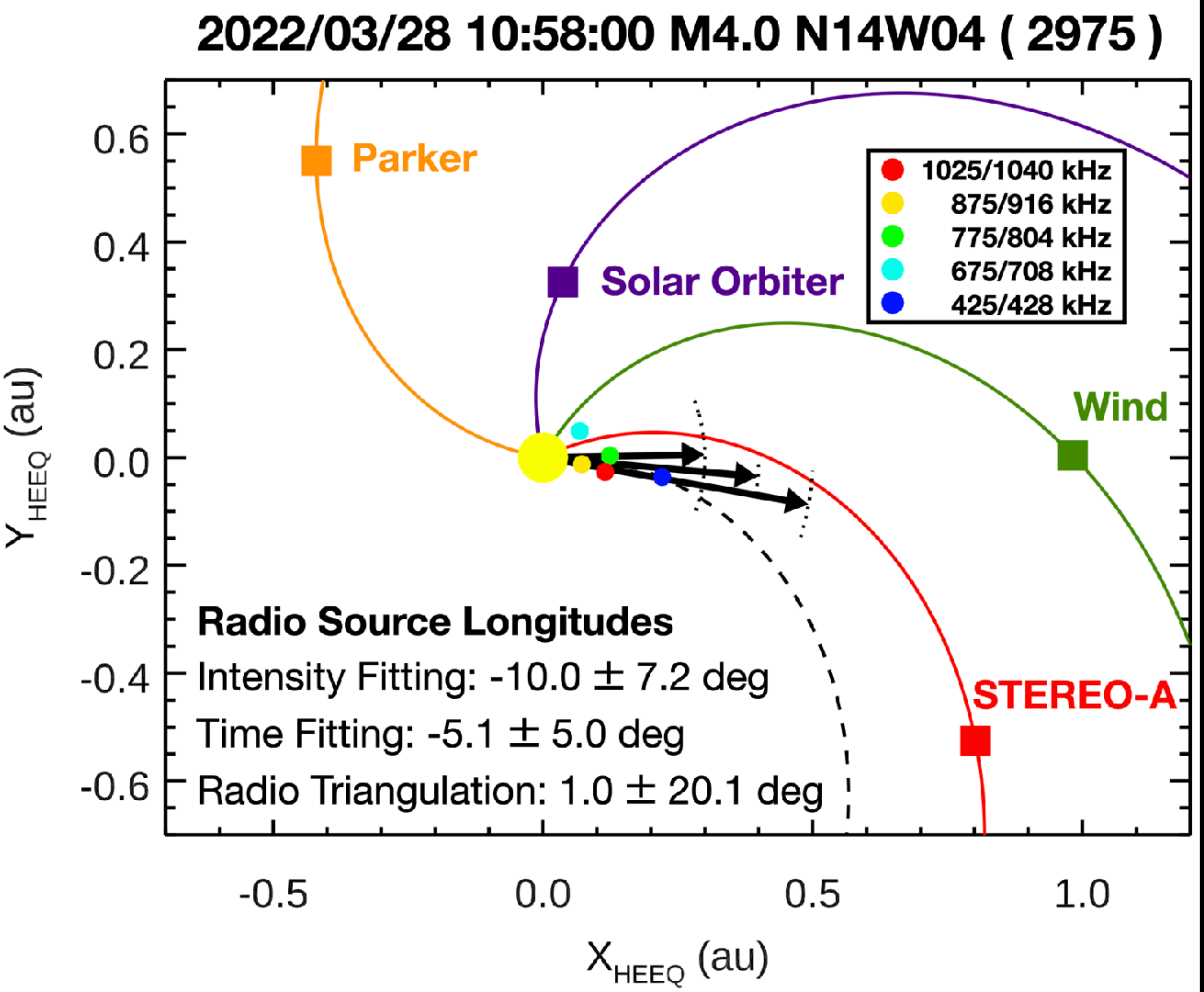

2022/03/28 10:58:00 M4.0 N14W04 (2975)
Parker
Solar Orbiter
Wind
STEREO-A
1025/1040 kHz
875/916 kHz
775/804 kHz
675/708 kHz
425/428 kHz
Radio Source Longitudes
Intensity Fitting: -10.0 ± 7.2 deg
Time Fitting: -5.1 ± 5.0 deg
Radio Triangulation: 1.0 ± 20.1 deg
0.6
0.4
0.2
0.0
-0.2
-0.4
-0.6
-0.5
0.0
0.5
1.0
Y_{HEEQ} (au)
X_{HEEQ} (au)

$$S(\lambda) = \frac{S_0}{\kappa} \exp\left(\kappa \cos(\lambda - \lambda_0)\right)$$

$$T(\lambda) = \frac{T_0}{\kappa} \exp\left(\kappa \sin(\lambda - \lambda_0)\right)$$

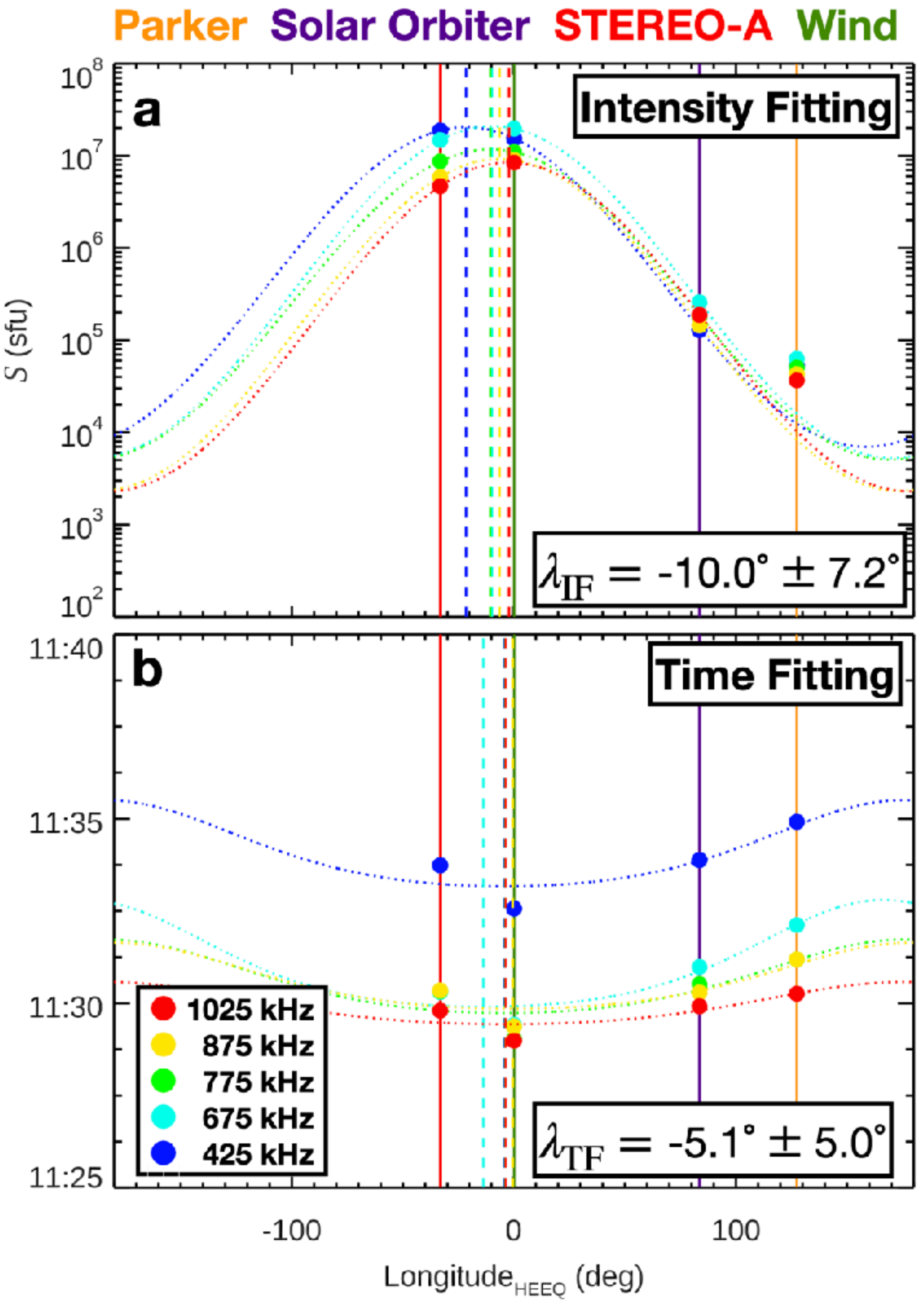

Solar Flares[a]							Type III Bursts[b]		
GOES Class	Date	Start	Stop	Peak	Position	NOAA[c]	Radio Flux[d]	Peak	Position[e]
M4.4	2020-11-29	12:34	13:41	13:11	S23°, E89°	n/a[f]	3×10^5	13:22	E84°
M1.1	2021-05-22	17:03	17:16	17:11	N18°, E18°	2824	2×10^5	17:12	E36°
M1.1	2021-05-23	11:00	11:14	11:08	N20°, E05°	2824	4×10^6	11:06	E23°
X1.5	2021-07-03	14:18	14:34	14:29	N23°, W82°	2838	1×10^5	14:32	W70°
M1.3	2021-10-26	02:40	02:54	02:47	N14°, E88°	n/a[g]	1×10^4	02:52	E81°
M1.0	2021-10-26	15:42	16:02	15:57	N13°, E89°	n/a[h]	1×10^4	15:56	E68°
X1.0	2021-10-28	15:17	15:48	15:35	S28°, W01°	2887	1×10^8	15:37	E03°
M1.8	2021-12-20	11:12	11:55	11:36	S20°, W01°	2908	2×10^4	11:39	E40°
M5.5	2022-01-20	05:41	06:12	06:01	N08°, W76°	2929	1×10^7	05:58	W13°
M4.0	2022-03-28	10:58	11:45	11:29	N14°, W04°	2975	8×10^6	11:29	E10°
X1.3	2022-03-30	17:21	17:46	17:37	N13°, W31°	2975	1×10^7	17:41	W16°
M9.6	2022-03-31	18:17	18:45	18:35	N12°, W47°	2975	3×10^5	18:42	W19°
X2.2	2022-04-20	03:41	04:04	03:57	S34°, W86°	2992	3×10^5	03:58	W75°
M6.7	2022-08-28	15:48	16:46	16:19	S30°, W85°	3088	2×10^5	16:08	W46°
M5.8	2022-10-01	19:58	20:16	20:10	N17°, W35°	3110	7×10^5	20:05	W16°
X1.0	2022-10-02	19:53	20:34	20:25	N17°, W49°	3110	2×10^5	20:23	W22°
M3.9	2022-10-11	08:36	08:46	08:42	N24°, W35°	3112	2×10^6	08:43	W10°

[a] Solar flare parameters from https://www.solarmonitor.org/

[b] at 1 MHz from *Wind*

[c] NOAA active regions are based on the NOAA/USAF Active Region Summary.

[d] in sfu

[e] derived from intensity fitting

[f] Events not associated with currently named NOAA regions

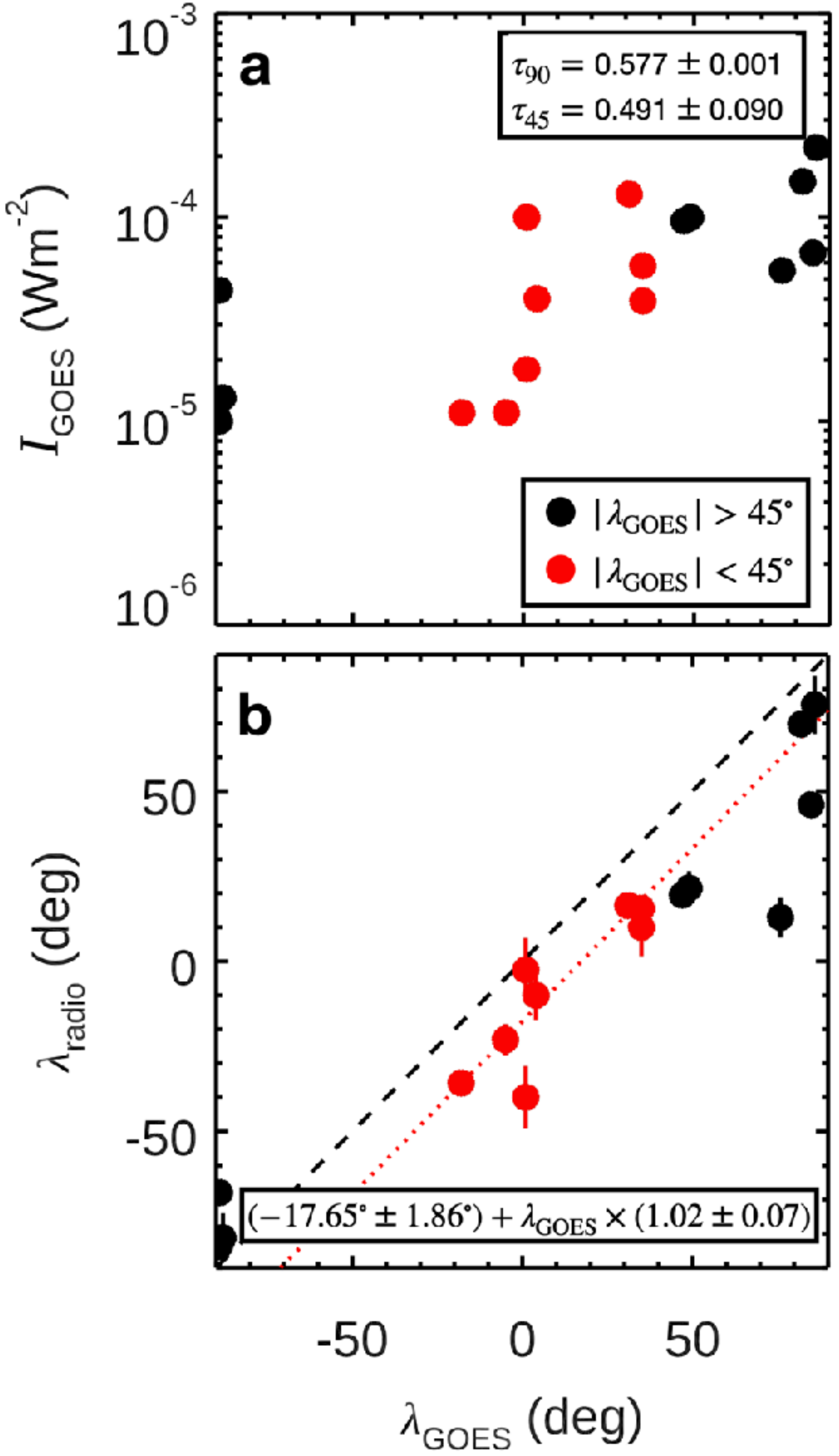

a
$\tau_{90} = 0.577 \pm 0.001$
$\tau_{45} = 0.491 \pm 0.090$
$|\lambda_{GOES}| > 45°$
$|\lambda_{GOES}| < 45°$
I_{GOES} (Wm^{-2})
10^{-3}
10^{-4}
10^{-5}
10^{-6}
b
$(-17.65° \pm 1.86°) + \lambda_{GOES} \times (1.02 \pm 0.07)$
λ_{radio} (deg)
50
0
-50
-50
0
50
λ_{GOES} (deg)

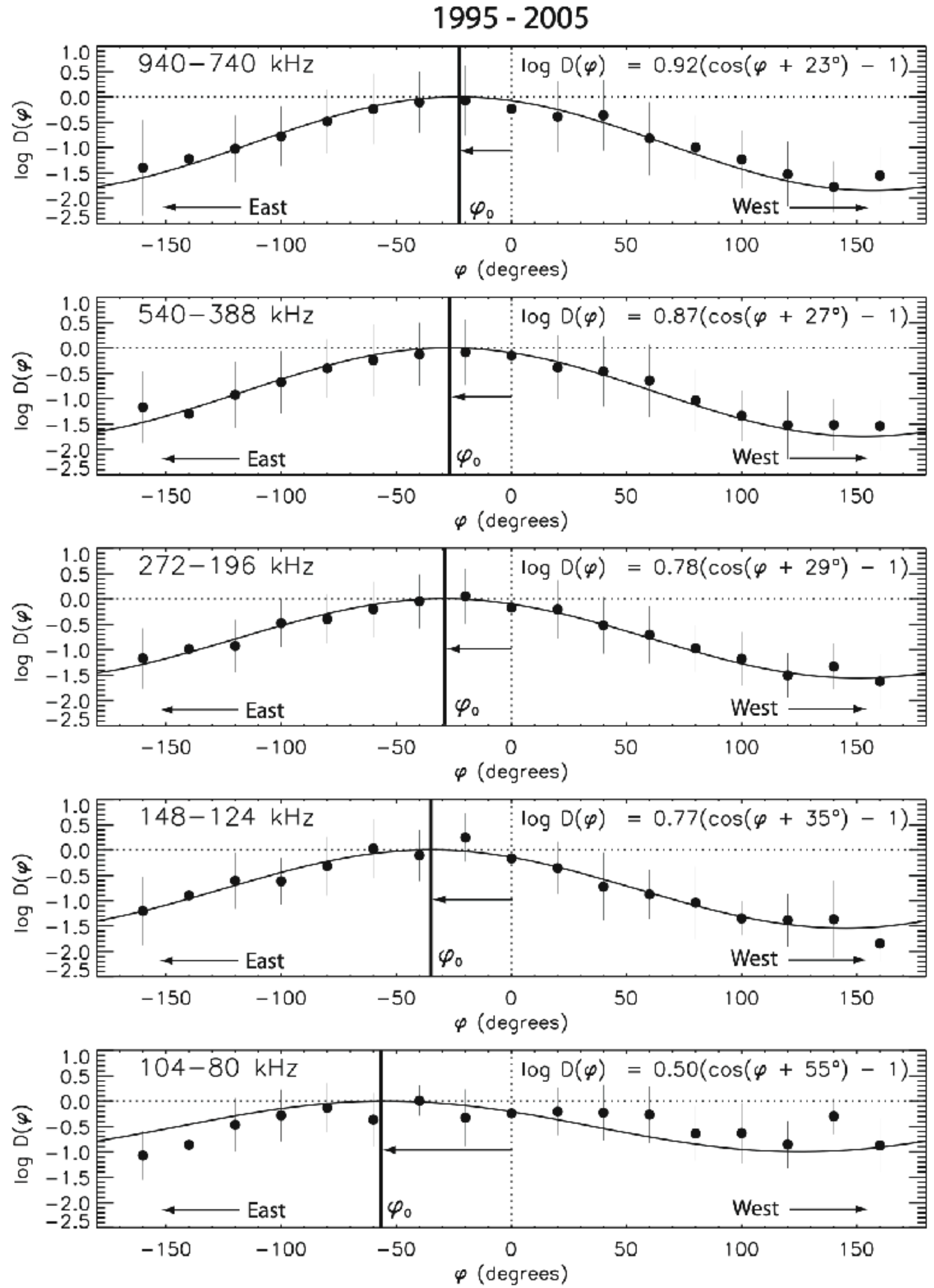

Bonnin et al. (2008)

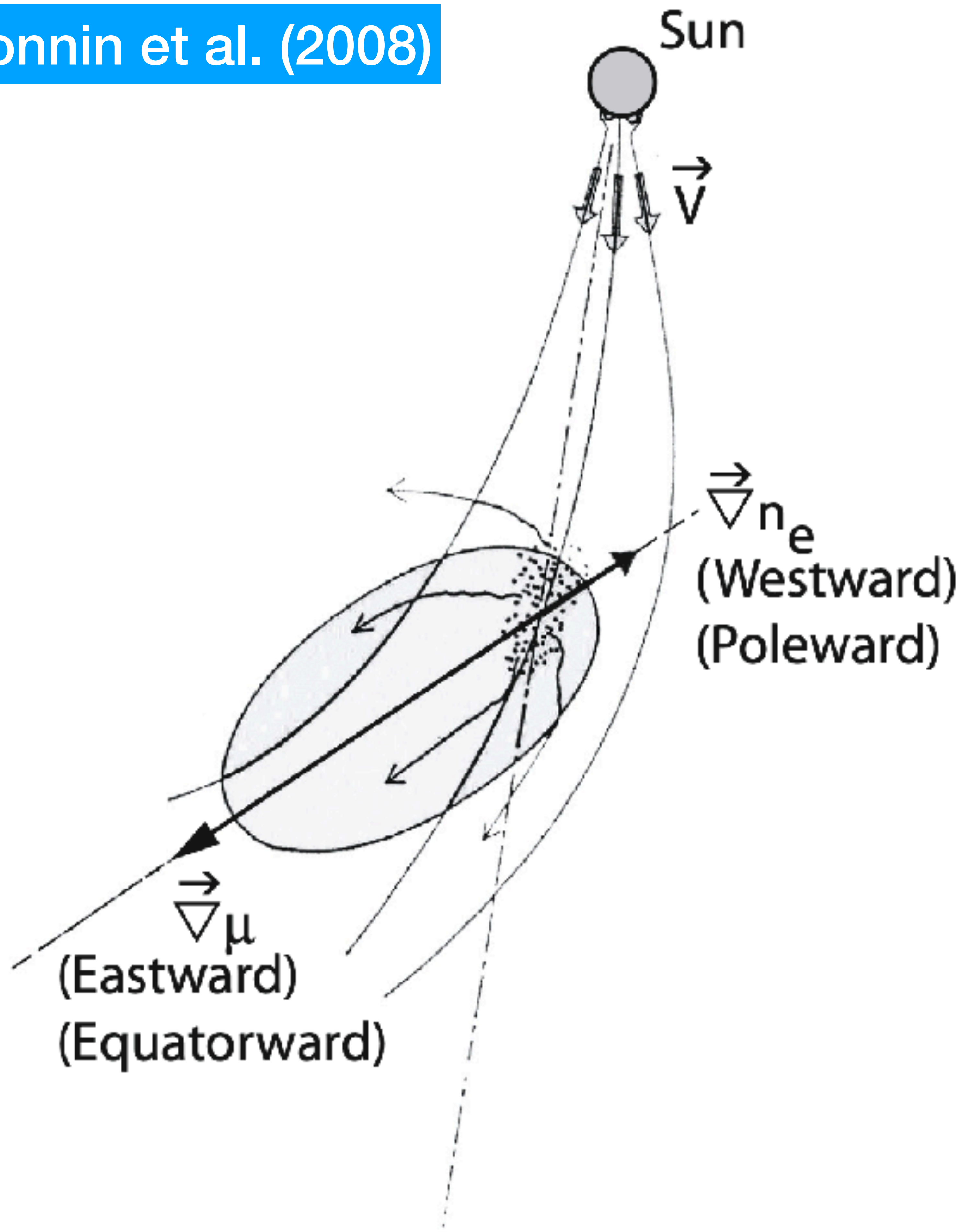

Fig. 6. Schematic interpretation of the eastward (equatorward) shift of the type III emission diagram in longitude (latitude) relative to the local open-field direction at the source. The type III electrons travel outward along spiral open-field lines from the associated flare sites in active regions. Along these paths, the solar wind escapes faster than in the surrounding areas filled with structures of closed-field lines. At some distance farther out, the faster wind catches up with the ambient slower wind and produces a density compression that leads to a transverse density gradient ∇n_e directed westward (poleward) of the open-field direction. This in turn results in a refractive index gradient $\nabla\mu = -\nabla n_e$, oriented eastward (equatorward) in the opposite sense of the density gradient. Radiation is thus bent in the eastward (equatorward) direction as observed.

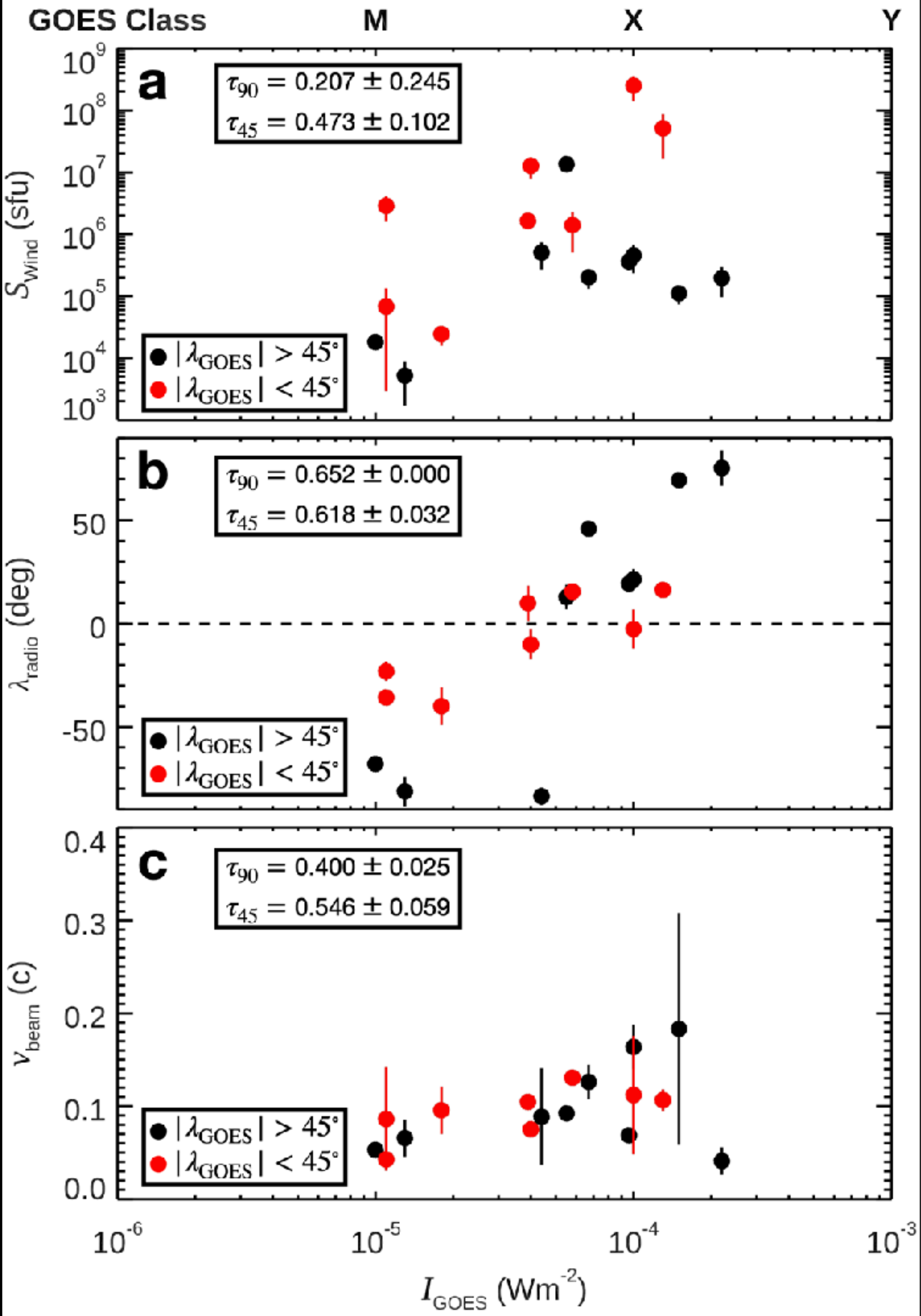

Krupar et al., ApJ, submitted

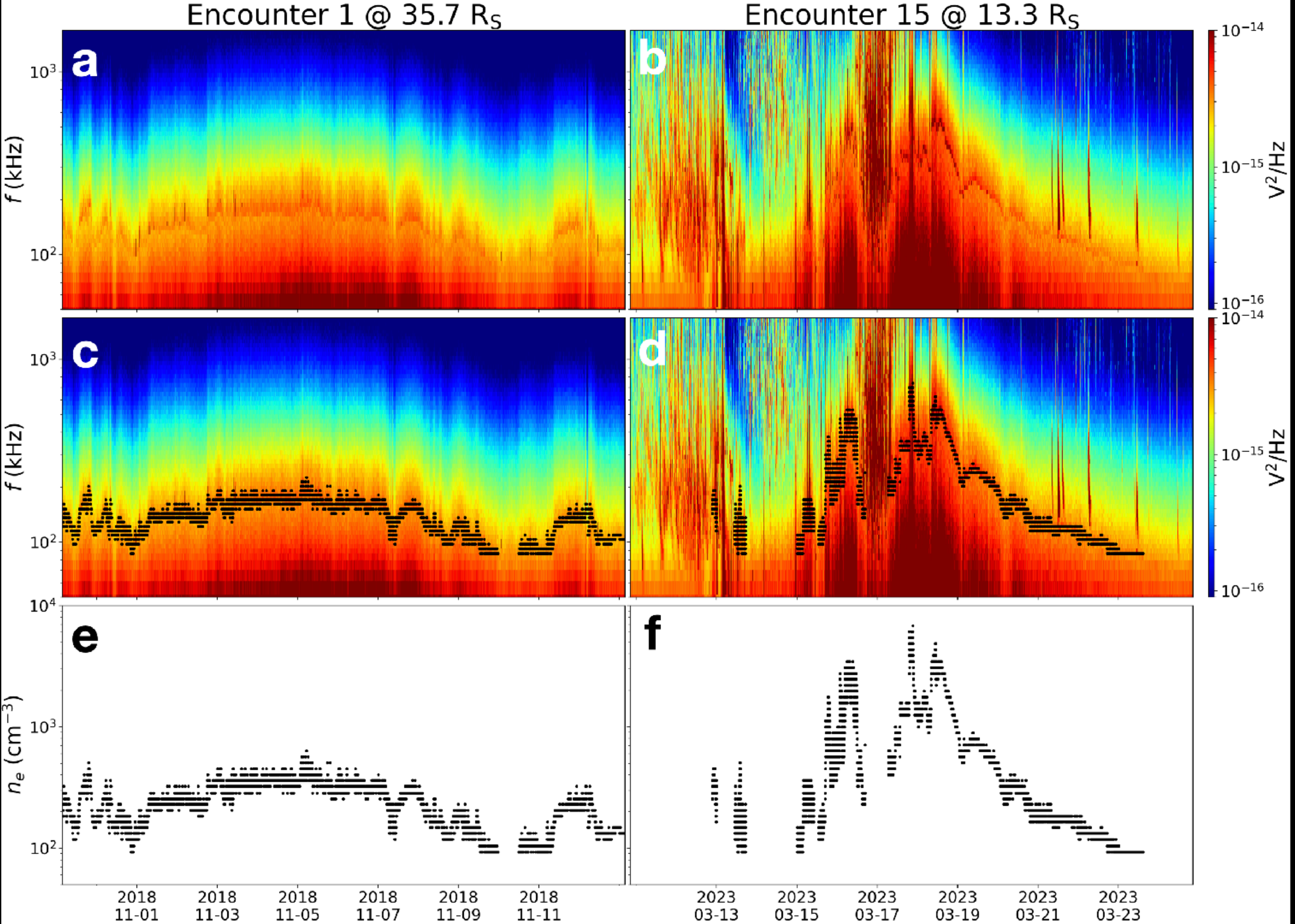

Encounter 1 @ 35.7 R_S
Encounter 15 @ 13.3 R_S
a
b
c
d
e
f
f (kHz)
V^2/Hz
n_e (cm^{-3})
2018 11-01
2018 11-03
2018 11-05
2018 11-07
2018 11-09
2018 11-11
2023 03-13
2023 03-15
2023 03-17
2023 03-19
2023 03-21
2023 03-23

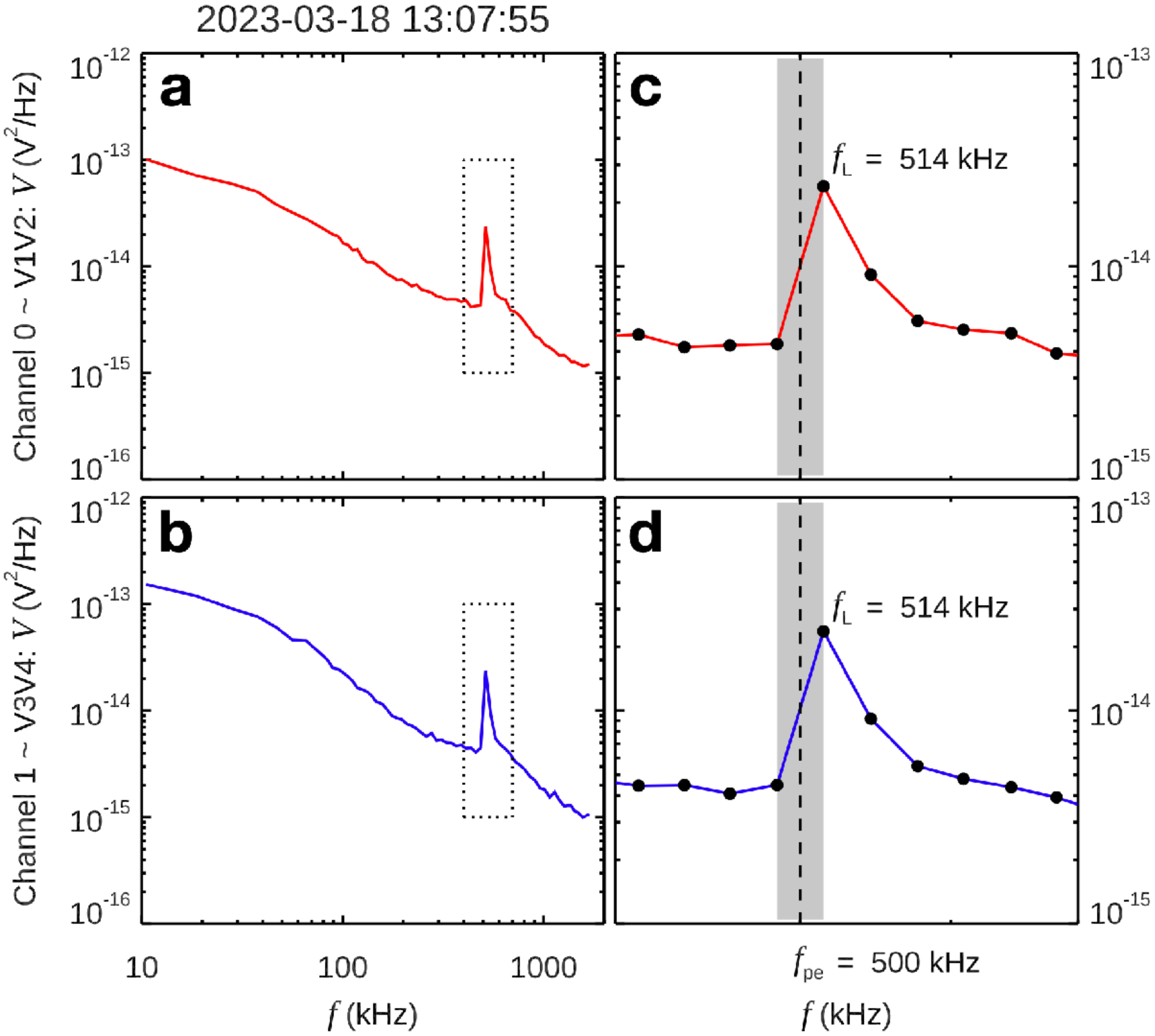

2023-03-18 13:07:55
a
b
c
d
Channel 0 ~ V1V2: V (V²/Hz)
Channel 1 ~ V3V4: V (V²/Hz)
10⁻¹²
10⁻¹³
10⁻¹⁴
10⁻¹⁵
10⁻¹⁶
fL = 514 kHz
fpe = 500 kHz
10
100
1000
f (kHz)
f (kHz)

QTN Density Profiles Across 15 Parker Solar Probe Encounters

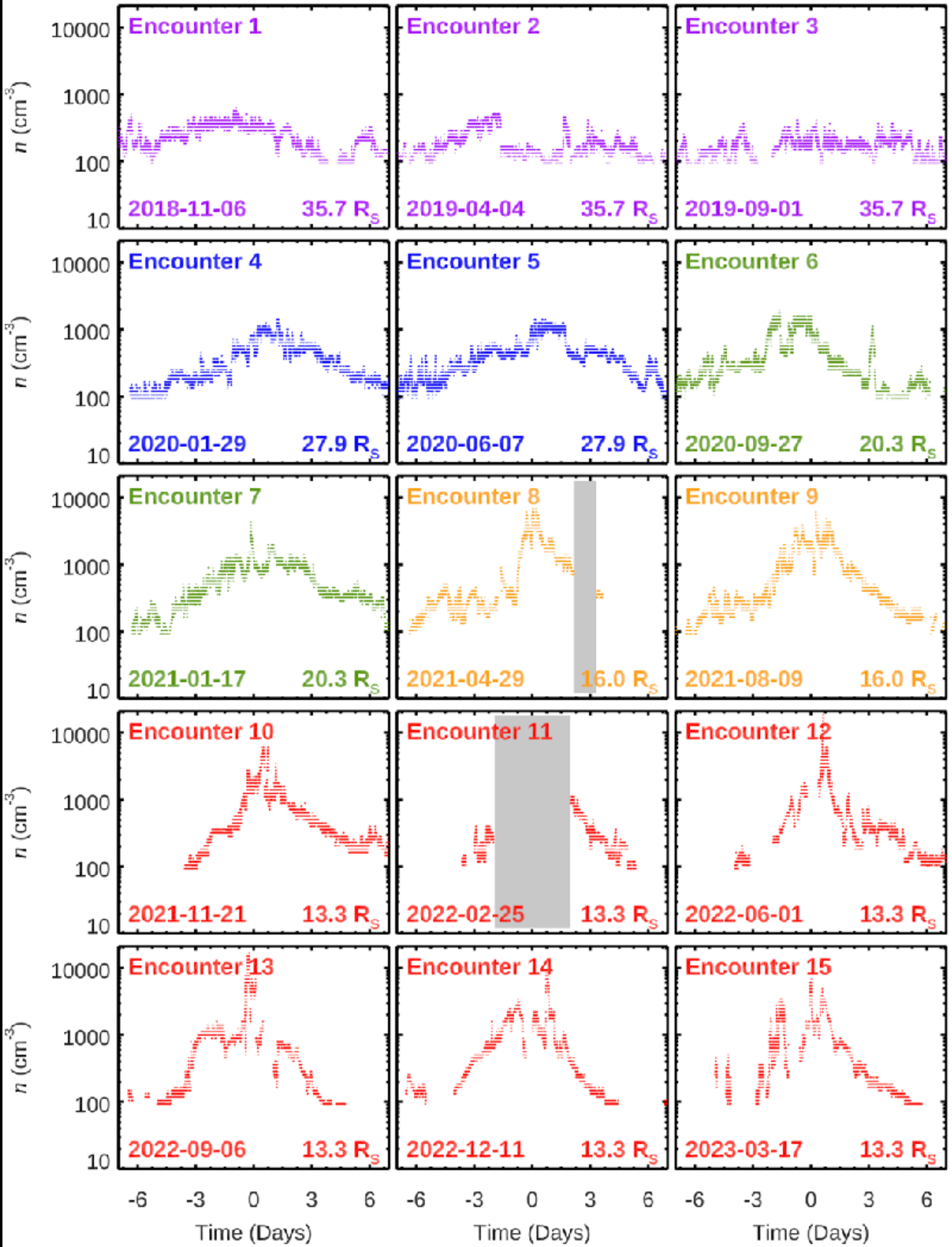

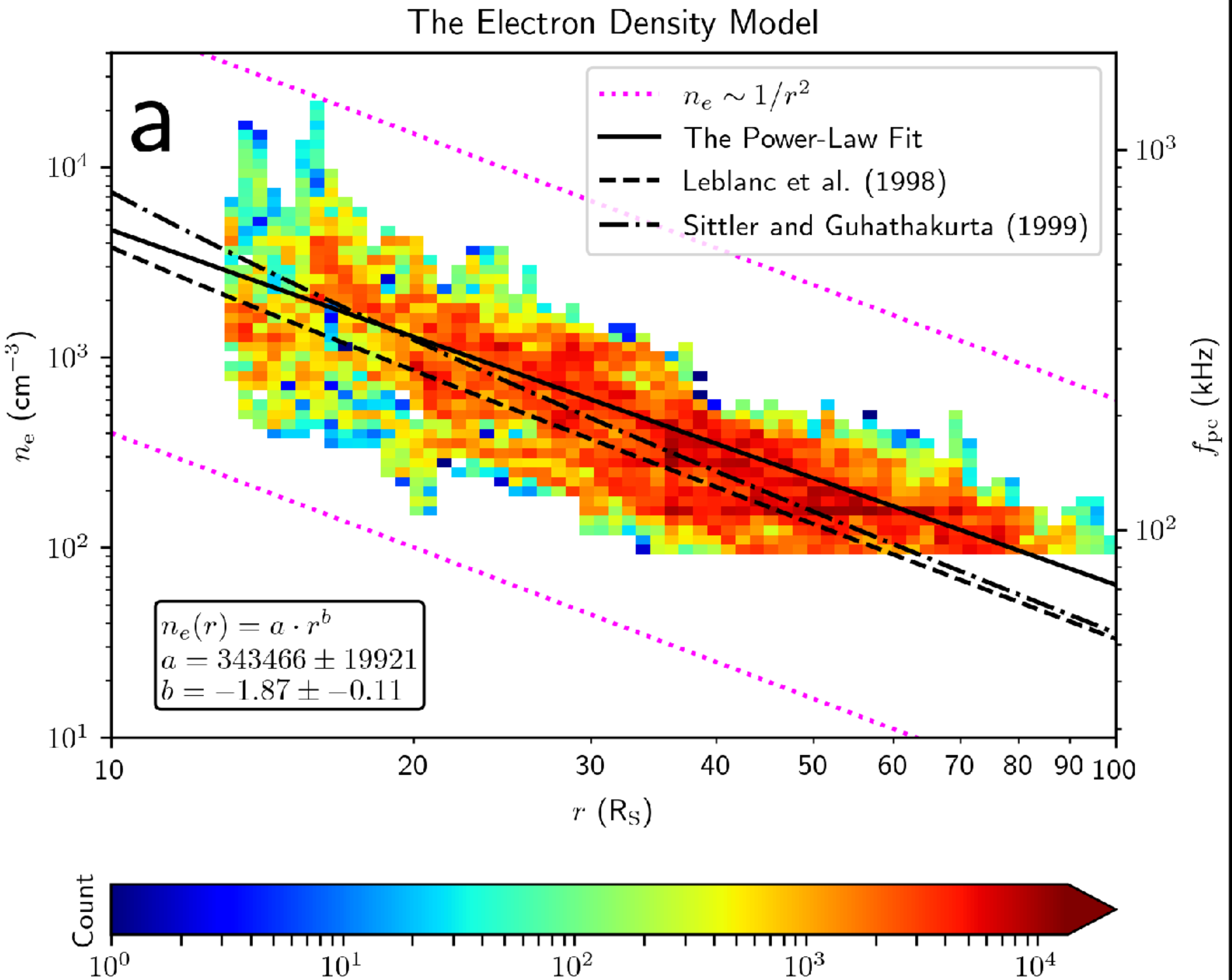

The Electron Density Model
a
$n_e \sim 1/r^2$
The Power-Law Fit
Leblanc et al. (1998)
Sittler and Guhathakurta (1999)
$n_e(r) = a \cdot r^b$
$a = 343466 \pm 19921$
$b = -1.87 \pm -0.11$
n_e (cm^{-3})
f_{pc} (kHz)
r (R_S)
Count

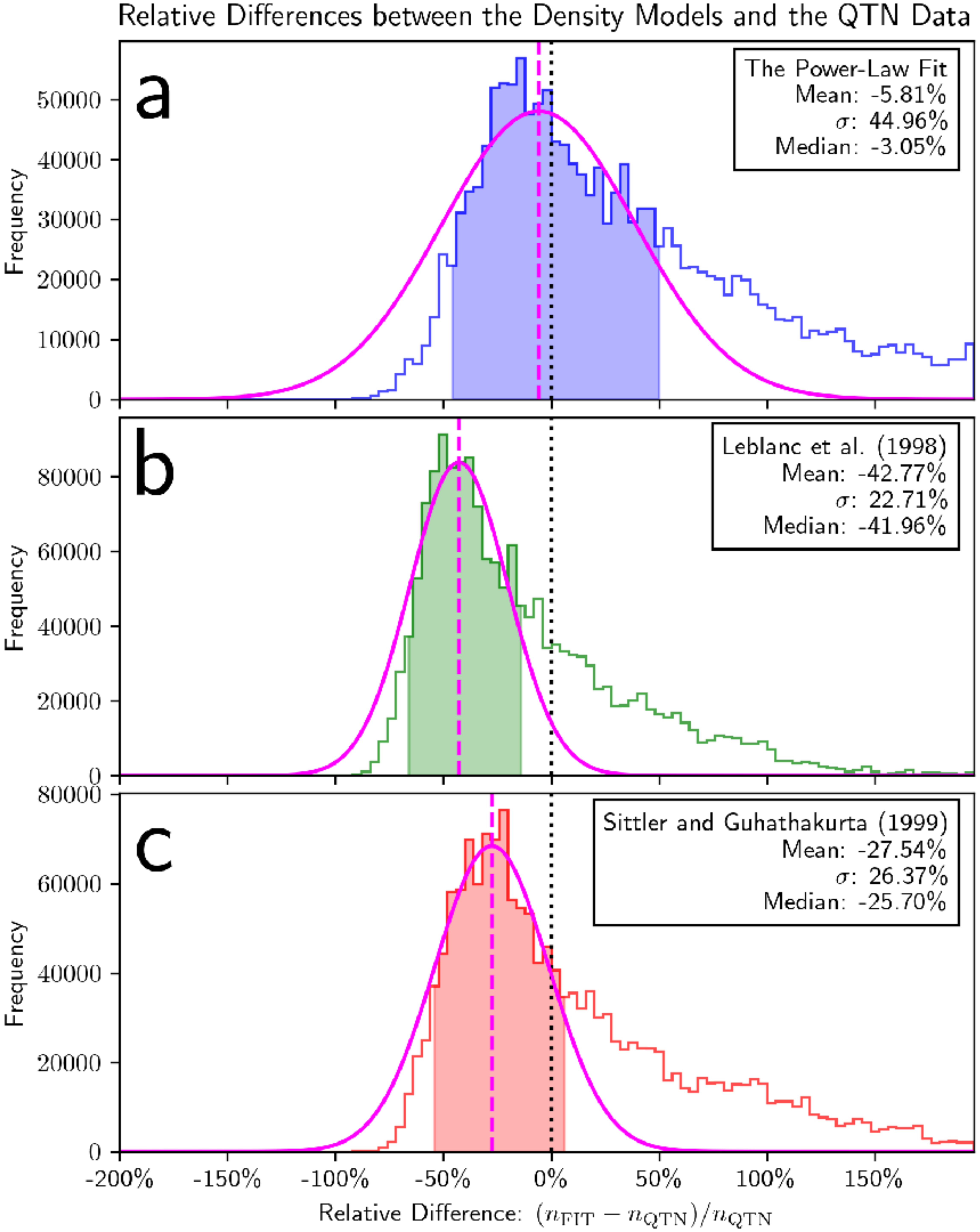

Kruparova et al., ApJ, accepted

https://spdf.gsfc.nasa.gov/pub/data/psp/fields/l3/rfs_lfr_qtn/